



## Modeling the Influence of Residual Stress on the Ultimate Load Conditions of Steel Frames

Barry T. Rosson<sup>1</sup>

### Abstract

A generalized material model for wide-flange sections was developed based on  $m$ - $p$ - $\tau$  plots of detailed fiber element models over a full range of moment, axial load and maximum residual stress conditions. Several different cross-sections were investigated to determine the appropriate exponent in the material model for approximating the stiffness reduction under major axis bending or minor axis bending conditions. The nonlinear material model was used as normalized tangent modulus expressions in *MASTAN2* and ultimate load analyses were conducted on four benchmark frames. Using residual stress scale factor conditions of 0.6 and 1.4, the relative percent difference in the lateral load at collapse was investigated as the initial vertical load conditions were increased. The influence of residual stress was studied on three test frames with loads applied only at the beam-to-column joints and on one test frame with more realistic design conditions. Discussion is provided on the ability of the material model to approximate the stiffness reduction of wide-flange sections and on the conditions that produce an increased residual stress effect on the ultimate load capacity of steel frames.

### 1. Introduction

The non-uniform cooling rate of W-Shapes after the rolling process creates initial longitudinal residual stresses in the cross-section. The ends of the flanges and center of the web cool much faster than the intersections of the flanges and web. This differential cooling produces residual stress profiles that vary such that maximum compression stresses occur at the flange tips and web center, and maximum tension stresses occur at the flange-web intersections. The magnitude and pattern of the residual stresses vary depending on the method of manufacture, country of origin, cross-section shape and material properties (Shayan *et al.* 2014). Dating back to the 1950's extensive laboratory testing has been conducted to measure the effects of residual stress on various structural steel shapes (Huber *et al.* 1954; Beedle *et al.* 1962; Spoorenberg *et al.* 2011; Shi *et al.* 2012; Ban *et al.* 2012 and 2013; Gardner *et al.* 2016). In order to model the residual stress as a random variable in advanced analyses of steel frames, Shayan *et al.* (2014) fit established residual stress patterns to experimental measurements found in the literature for residual stresses over the cross-section. Using the ECCS (1984) residual stress pattern in Fig. 1, their approach used a random scale factor  $X$  using a total of 63 residual stress measurements. Scale factors were derived

---

<sup>1</sup> Professor, Florida Atlantic University, <rosson@fau.edu>

by error minimization of the theoretical residual stress pattern and the non-dimensionalized experimental measurements. A normal distribution was fit to histograms of the derived scale factors for the ECCS residual stress pattern, and statistics revealed a mean scale factor  $\mu_X = 1.047$  and coefficient of variation  $COV = 0.210$ .

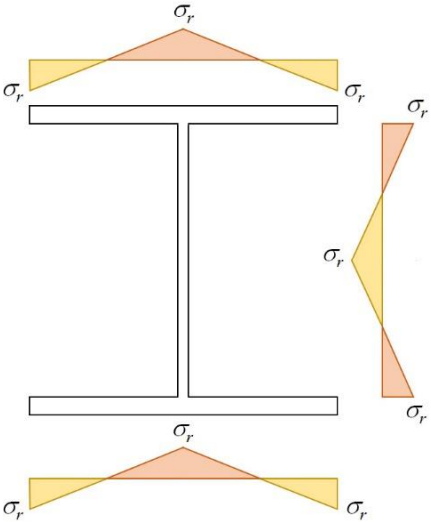


Figure 1: ECCS residual stress pattern

The purpose of this study is to investigate the effect of residual stress magnitude on the ultimate load capacity of steel frames. As depicted in Fig. 2, Shayan *et al.* (2014) performed their study based on scale factors that varied by a maximum of two standard deviations of the mean. Since  $\mu_X$  and  $COV$  are very close to 1 and 0.20, respectively, scale factors of 0.6 and 1.4 were chosen for their computer models, and thus they were also used in the current study. A mean residual stress of  $0.3\sigma_y$  was used for all cross-sections; thus the maximum residual stress  $\sigma_r$  is  $0.18\sigma_y$  for the scale factor 0.6, and  $0.42\sigma_y$  for the scale factor 1.4.

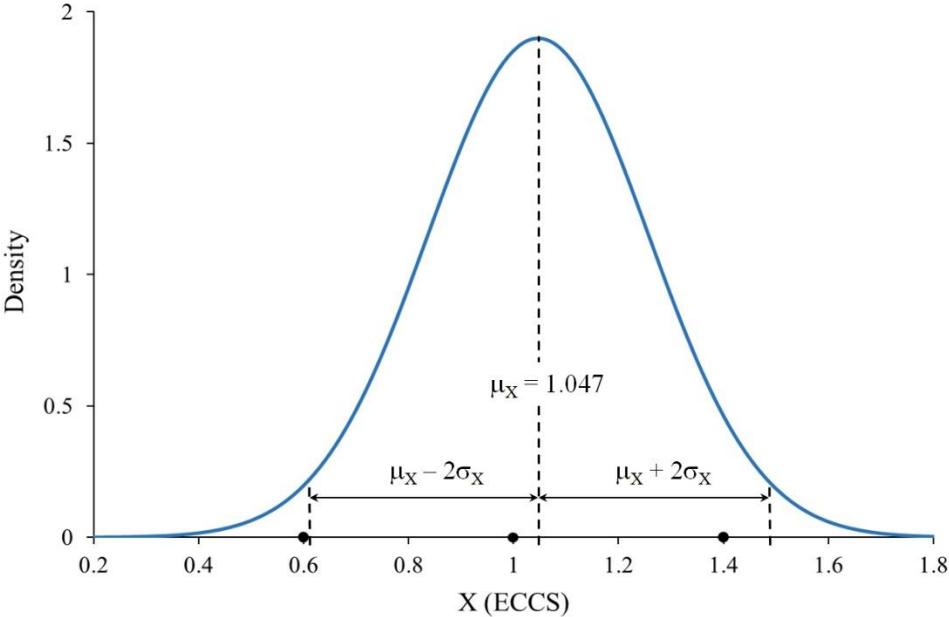


Figure 2: Residual stress statistics of ECCS model by Shayan *et al.*

## 2. Axial Compression $m$ - $p$ - $\tau$ Surface Plots

The stiffness reduction ( $\tau$ ) that results from yielding of the cross-section due to bending and axial load was studied in detail using a fiber element model for W-Shapes with an ECCS residual stress pattern as depicted in Fig. 1 (Rosson 2017). The model used 2,046 fiber elements over the cross-section (400 fiber elements in each flange and 1,246 fiber elements in the web). For a given normalized moment  $m$  ( $M/M_p$ ), axial load  $p$  ( $P/P_y$ ), and residual stress ratio  $c_r$  ( $\sigma_r/\sigma_y$ ), the stiffness reduction was carefully assessed for a W8x31 with  $c_r = 0.3$ . Throughout the paper  $p$  is understood to be positive such that the sign on  $P_y$  matches that of the applied axial load  $P$ . Bending about the minor axis is understood to have a normalized moment  $m = M/M_{py}$ , and bending about the major axis is understood to have a normalized moment  $m = M/M_{px}$ .

Using the  $m$  and  $p$  results with increments of 0.01, over 7,000 data points were used to produce the  $m$ - $p$ - $\tau$  surface plot in Fig. 3 for minor axis bending and axial compression, and in Fig. 4 for major axis bending and axial compression.

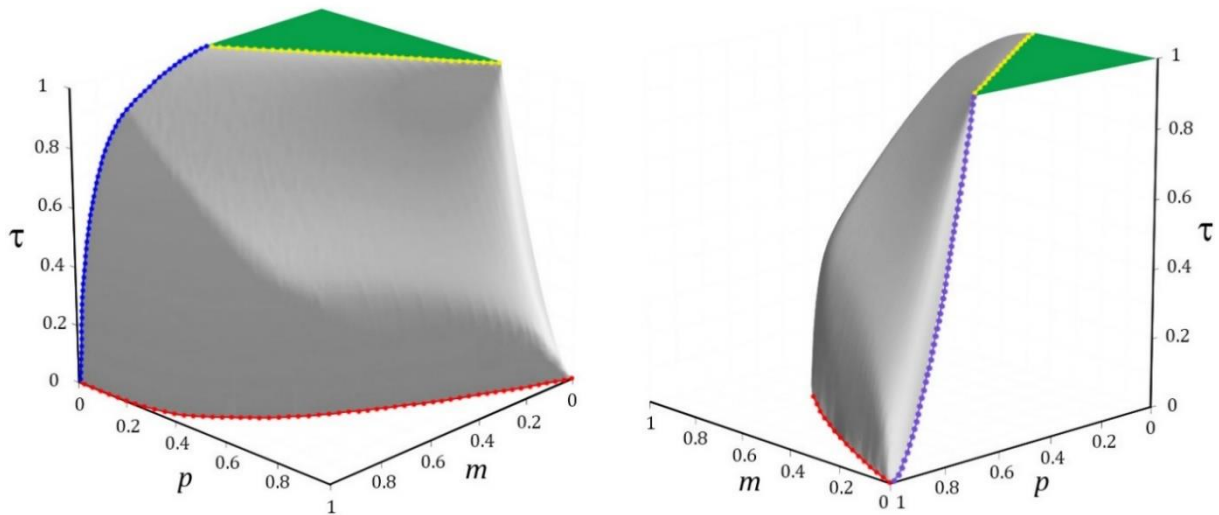


Figure 3: W8x31 minor axis bending and axial compression  $m$ - $p$ - $\tau$  surface plot perimeter conditions for  $c_r = 0.30$

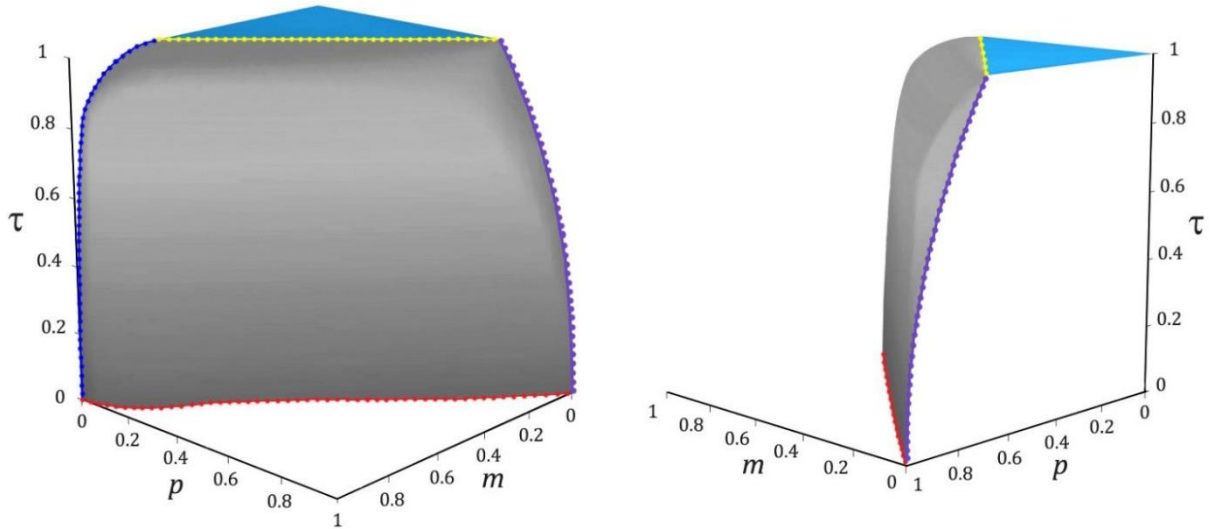


Figure 4: W8x31 major axis bending and axial compression  $m$ - $p$ - $\tau$  surface plot perimeter conditions for  $c_r = 0.30$

### 2.1 Yellow line ( $m$ and $p$ conditions at the limit of $\tau = 1$ )

The equation to determine the extent of  $\tau = 1$  is found in the literature (Attalla *et al.* 1994; Zubydan 2011) and is depicted in Fig. 5 for the minor axis bending and axial compression condition. The dashed blue lines represent the residual stress distribution, and the shaded region represents the final compression stresses across each flange after the bending moment and axial load have been applied. The left side of the diagram depicts the accumulation of three stresses: the residual compression stress  $\sigma_r$ , the bending moment compression stress  $\sigma_m$ , and the axial compression stress  $\sigma_p$ . The extent of  $\tau = 1$  is determined when the conditions of  $m$  and  $p$  cause all three compression stresses to sum to  $\sigma_y$ . For a given residual stress ratio  $c_r$  and axial compression load condition  $p$ , the maximum moment at which  $\tau = 1$  is maintained is given as

$$m_1 = \frac{S_y}{Z_y} (1 - c_r - p) \quad (1)$$

where  $S_y$  is the minor axis elastic section modulus and  $Z_y$  is the minor axis plastic section modulus. Since this equation is based only on the accumulation of stress at the end of each flange, the assumed shape of the residual pattern does not affect Eq. 1 provided the maximum residual compression stress  $\sigma_r$  occurs at the end of the flanges.

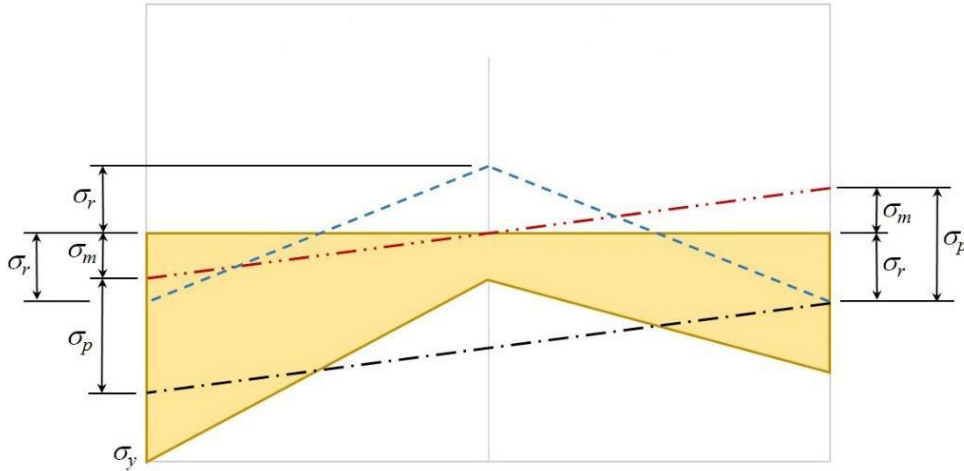


Figure 5: Minor axis bending stress state in the flanges at the extent of  $\tau = 1$

The maximum moment at which  $\tau = 1$  is maintained for the major axis bending and axial compression condition is determined in a similar manner and is found to be

$$m_1 = \frac{S_x}{Z_x} (1 - c_r - p) \quad (2)$$

where  $S_x$  is the major axis elastic section modulus and  $Z_x$  is the major axis plastic section modulus. Since this equation is based only on the accumulation of stress at the outer edge of the flange, the assumed shape of the residual pattern does not affect Eq. 2 provided the maximum residual compression stress  $\sigma_r$  occurs at this location.

### 2.2 Purple line ( $m = 0$ and $p > 1 - c_r$ )

The equation to determine the stiffness reduction when  $m = 0$  is found by considering the stress state depicted in Fig. 6. The compressive stress  $\sigma_p'$  that satisfies the equilibrium condition for a given  $p$  and  $c_r$  condition provides the necessary information to determine the extent of yielding over the length  $h_y$  at the ends of the flanges and over the length  $2h_y$  at the center of the web. To determine the stiffness reduction  $\tau$  for a given  $p$  and  $c_r$  condition, the minor axis moment of inertia of the remaining cross-section that has not yielded is divided by the original minor axis moment of inertia  $I_y$ . The relationship for  $\tau$  is found to be

$$\tau_p = \frac{2 \left( \sqrt{\frac{1-p}{c_r}} \right)^3 + \lambda \lambda_o^2 \sqrt{\frac{1-p}{c_r}}}{2 + \lambda \lambda_o^2} \quad (3)$$

where  $\lambda = A_w/A_f$  and  $\lambda_o = t_w/b_f$ . For W-Shapes in which  $\lambda \lambda_o^2$  is very small compared to 2, a very close approximation to Eq. 3 excludes the effect of the web and is given as

$$\tau_p = \left( \sqrt{\frac{1-p}{c_r}} \right)^3 \quad (4)$$

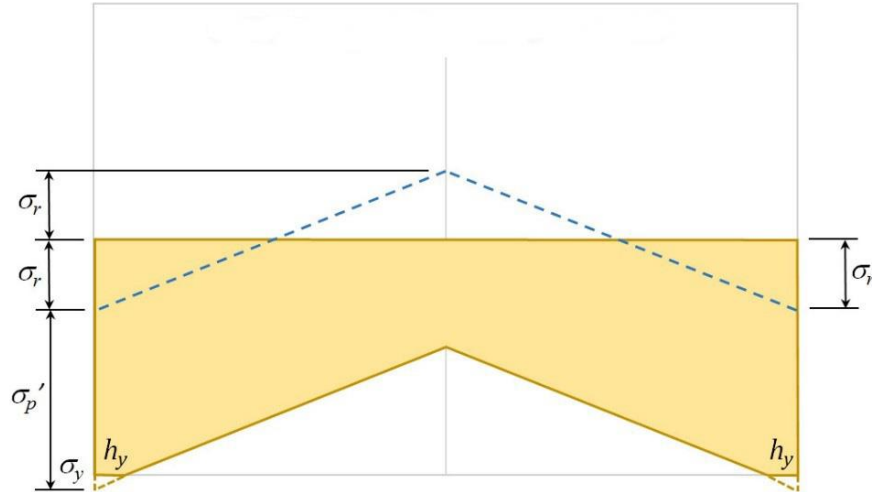


Figure 6: Minor axis bending stress state in the flanges for  $m = 0$

The stiffness reduction  $\tau$  for the major axis condition is determined in a similar manner and is found to be

$$\tau_p = \frac{\lambda \lambda_1^2 \left[ 1 - \left( 1 - \sqrt{\frac{1-p}{c_r}} \right)^3 \right] + \sqrt{\frac{1-p}{c_r}} [2 + 6(1 + \lambda_1)^2]}{\lambda \lambda_1^2 + 2 + 6(1 + \lambda_1)^2} \quad (5)$$

where  $\lambda_1 = d_w/t_f$ . Eqs. 3 through 5 are based entirely on the assumed shape of the residual pattern; therefore, the shape of the purple lines in Figs. 2 and 3 are unique to the ECCS residual stress pattern given in Fig. 1 (Rosson 2016 and 2017).

### 2.3 Red line ( $m$ and $p$ conditions for $\tau = 0$ )

Two equations are needed to determine the  $m$  and  $p$  conditions when  $\tau = 0$  for both minor and major axis bending. For the minor axis bending with axial compression condition, one equation is needed when the plastic neutral axis is inside the web thickness, and the other equation is needed when it is outside the web thickness. Closed-form equations are given in the book by Chen and Sohal (1995); however, the same results can be obtained with fewer computations using the constants  $\lambda$ ,  $\lambda_o$  and  $\lambda_1$  (Rosson 2016).

$$m_0 = 1 - \frac{p^2(2 + \lambda)^2}{(2 + \lambda\lambda_o)(2 + \lambda_1)} \quad (6)$$

$$\text{when } p \geq \frac{2\lambda_o + \lambda}{2 + \lambda} \quad m_0 = \frac{4 - [p(2 + \lambda) - \lambda]^2}{2(2 + \lambda\lambda_o)} \quad (7)$$

For the major axis bending with axial compression condition, one equation is needed when the plastic neutral axis is outside the flange thickness, and the other equation is needed when it is inside the flange thickness.

$$m_0 = 1 - \frac{p^2(2 + \lambda)^2}{4\lambda_o + \lambda(4 + \lambda)} \quad (8)$$

$$\text{when } p \geq \frac{\lambda}{2 + \lambda} \quad m_0 = \frac{(2 + \lambda_1)^2 - [p(2 + \lambda) - \lambda + \lambda_1]^2}{4 + \lambda_1(4 + \lambda)} \quad (9)$$

Eqs. 6 through 9 do not depend upon the assumed shape of the residual pattern; therefore, the shape of the red lines in Figs. 2 and 3 are unaffected by the ECCS residual stress pattern (Rosson 2017).

### 3. Material Model Based on $m$ - $p$ - $\tau$ Surface Plots

The equations presented for the yellow, purple and red lines in Figs. 3 and 4 are used as a basis to develop an inelastic material model for wide-flange sections. The extent of the triangular-shaped plateau region at which  $\tau = 1$  for a given  $p$  and  $c_r$  condition is defined by  $m_1$  from Eqs. 1 and 2. The stiffness when  $m = 0$  for a given  $p > 1 - c_r$  condition is defined by  $\tau_p$  from Eqs. 3 and 5, and the conditions at which  $\tau = 0$  for a given  $p$  condition are defined by  $m_0$  from Eqs. 6 through 9. For the  $m$  and  $p$  conditions between  $\tau = 1$  and  $\tau = 0$ , the shape of the 3D surface is dependent upon the given  $c_r$  condition of the ECCS residual stress pattern in Fig. 1. Equations for  $\tau$  in this region require an iterative procedure, thus approximate nonlinear  $\tau$  expressions are used instead. Taking advantage of the closed-form equations for  $m_1$ ,  $\tau_p$  and  $m_0$ , the 3D surfaces for both the minor axis bending and major axis bending conditions are closely approximated using Eqs. 10 and 11. An appropriate value for the exponent  $n$  is selected based on the fiber element results for a given wide-flange section and the axis about which bending occurs.

$$\tau = 1 - \left( \frac{m - m_1}{m_0 - m_1} \right)^n \quad (10)$$

$$\text{when } p \geq 1 - c_r \quad \tau = \tau_p \left[ 1 - \left( \frac{m}{m_0} \right)^n \right] \quad (11)$$

Various researchers have developed stiffness reduction models (Zubydan *et al.* 2011; Kucukler *et al.* 2014 and 2016); however, Eqs. 10 and 11 allow for direct input of the  $c_r$  condition. For a given  $m$ ,  $p$  and  $c_r$  condition, the stiffness reduction can be easily evaluated from the  $m_1$ ,  $\tau_p$  and  $m_0$  values from Eqs. 1, 3, 6 and 7 for minor axis bending, and Eqs. 2, 5, 8 and 9 for major axis bending. The ability of Eqs. 10 and 11 to approximate the actual  $m$ - $p$ - $\tau$  surface conditions are illustrated in Figs. 7 and 8 for a W8x31 with  $c_r = 0.3$  under major axis bending and minor axis bending conditions.

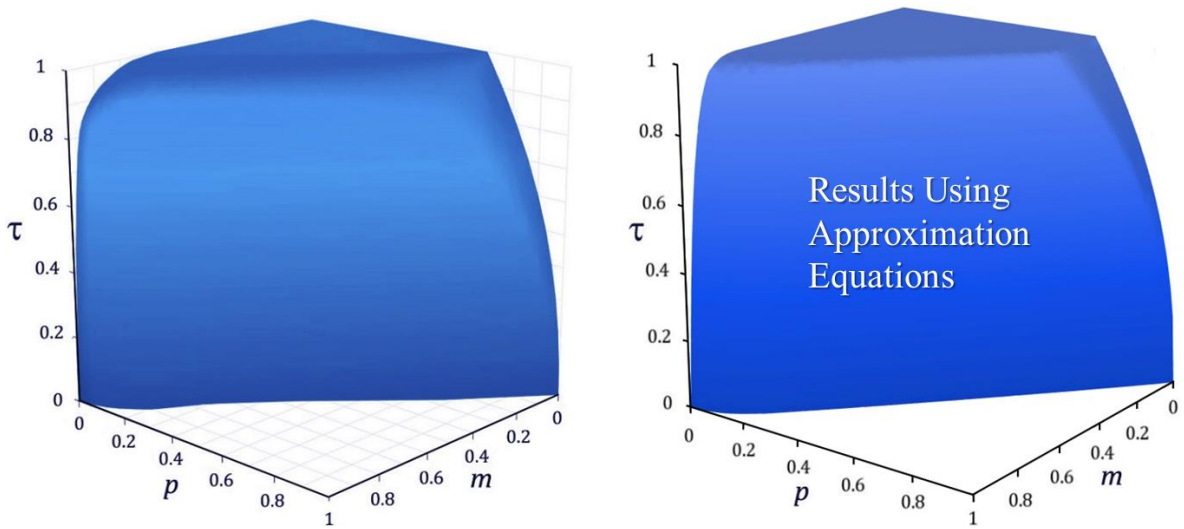


Figure 7: W8x31 major axis bending and axial compression  $m$ - $p$ - $\tau$  surface plots for  $c_r = 0.30$  and  $n = 8$

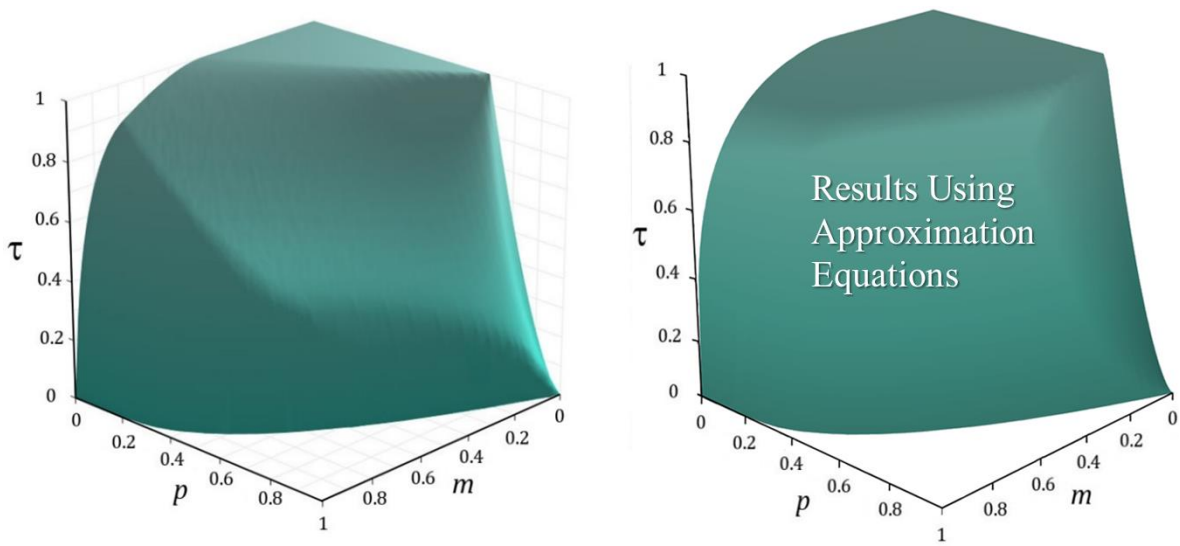


Figure 8: W8x31 minor axis bending and axial compression  $m$ - $p$ - $\tau$  surface plots for  $c_r = 0.30$  and  $n = 2$

The ability of Eqs. 10 and 11 to approximate the stiffness reduction is further illustrated in Fig. 9 for major axis bending over the full range of axial compression conditions. Comparing the moment-curvature diagrams based on the fiber element data with the approximate equation results, there is very close agreement when  $n = 8$  is used. Since  $m_1$  and  $\tau_p$  are in Eqs. 10 and 11, the moment-curvature plots will always match the fiber element results in the linear region up to the initial yield conditions, and since  $m_0$  is used, the approximate results will always converge to the fiber element results as the curvature increases for a given axial load condition.

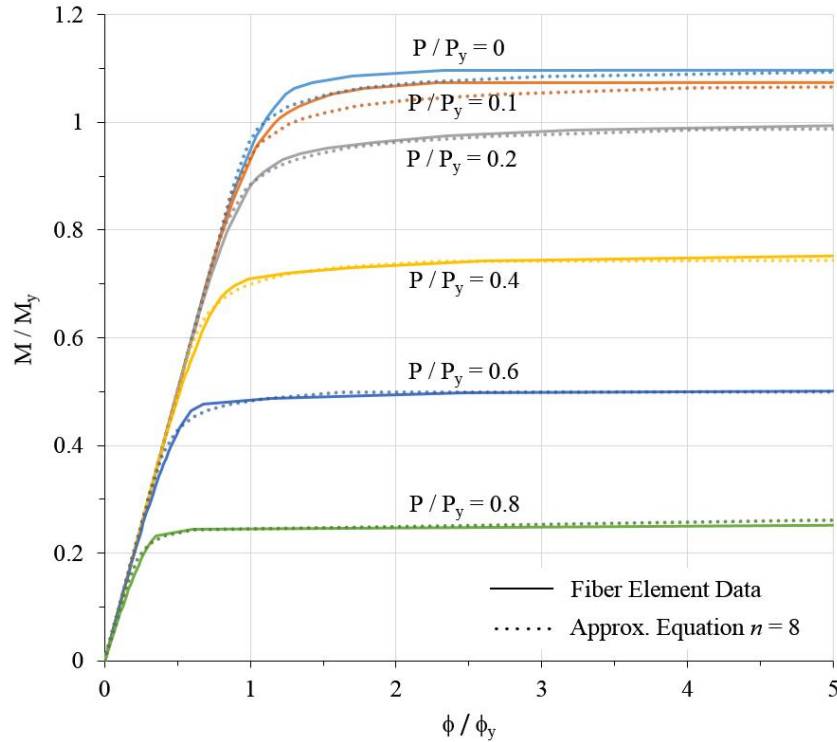


Figure 9: W8x31 major axis bending and axial compression moment-curvature plots for  $c_r = 0.30$

Fig. 10 illustrates the ability of Eqs. 10 and 11 to approximate the stiffness reduction for minor axis bending over the full range of axial compression conditions. Comparing the moment-curvature diagrams based on the fiber element data with the approximate equation results, the closest agreement occurs when  $n = 2$  is used. As before since  $m_1$  and  $\tau_p$  are in Eqs. 10 and 11, the moment-curvature plots will always match the initial yield conditions, and since  $m_0$  is used, the approximate results will always converge to the fiber element results as the curvature increases for a given axial load condition. The reason for the difference between the fiber elements results and approximate results in Fig. 10 is illustrated in Fig. 11 where it is evident that the shape of the  $m$ - $\tau$  curves vary significantly depending upon the magnitude of the axial load. Comparing the fiber element results in Figs. 7 and 8, it is noticed that this variation occurs only for the minor axis bending condition. Thus approximating the reduced stiffness will always have more error associated with the minor axis bending condition than for the major axis bending condition. Selecting different values of  $n$  will tend to reduce the error over a certain range of axial load conditions, but it will also simultaneously increase the error over the remaining range axial load conditions. For the W8x31 under minor axis bending conditions, selecting  $n = 2$  minimized the error as best as possible over the full range of axial load conditions.

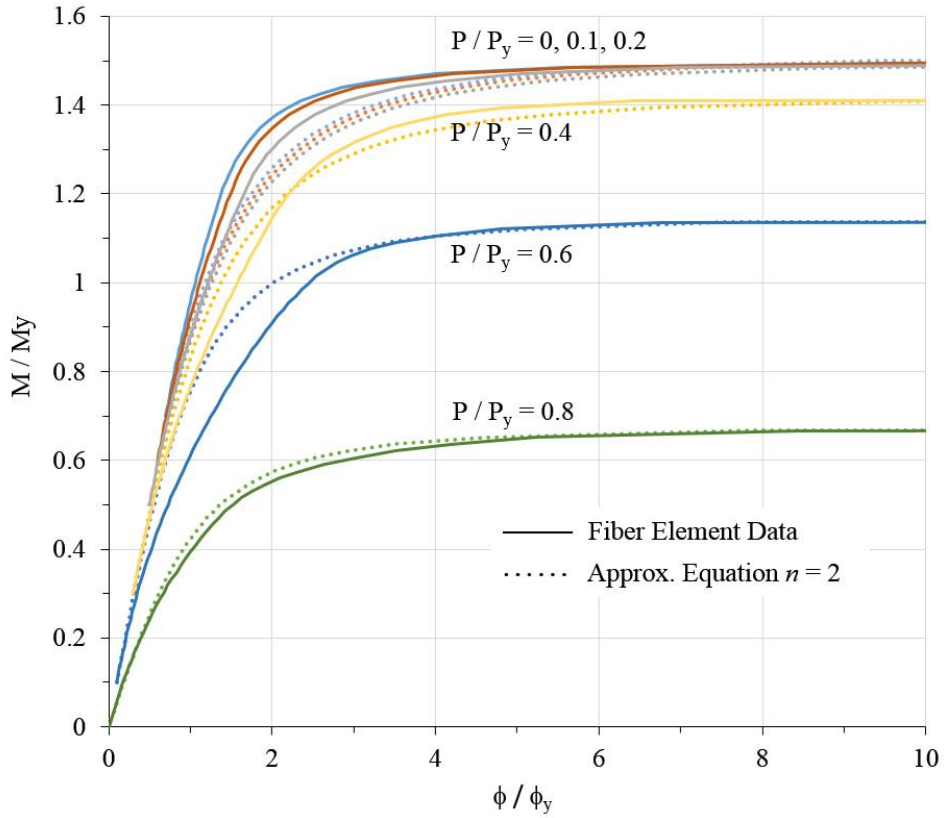


Figure 10: W8x31 minor axis bending and axial compression moment-curvature plots for  $c_r = 0.30$

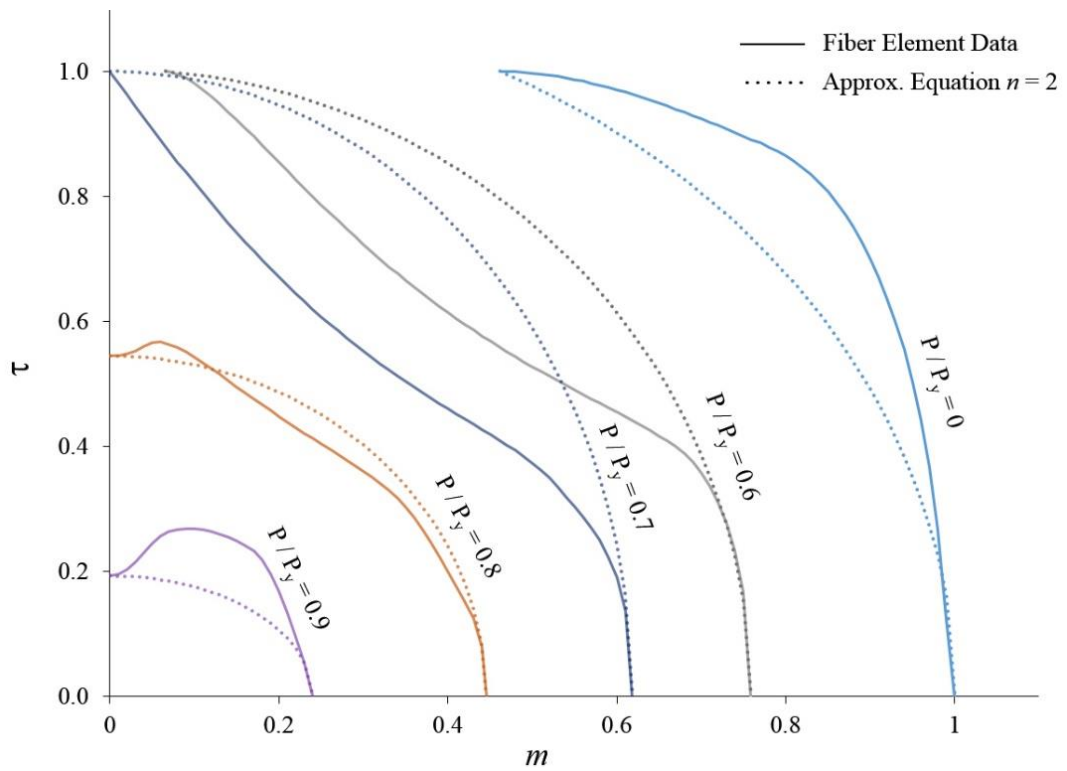


Figure 11: W8x31 minor axis bending and axial compression  $m$ - $\tau$  plots for  $c_r = 0.30$

#### 4. Influence of Residual Stress on the Ultimate Load Conditions of Test Frames

The El-Zanaty (1980) and Shayan (2014) test frames were used to study the influence of the magnitude of residual stress on the ultimate load conditions of steel frames. All of the cross-sections are assumed to be fully-compact and their out-of-plane behavior is fully restrained.

##### 4.1 Stiffness matrix used for modeling the distributed plasticity

Since the bending moments usually vary along the length of the beam-column, the stiffness reduction over the member length must also be accounted for when yielding occurs. An easy and effective way of accomplishing this is to assume the tangent modulus varies linearly over the length of the element. In practice, the error introduced by this assumption is reduced by using multiple elements along the length of the beam-column. The closed-form stiffness matrix developed by Ziemian and McGuire (2002) was used for this study because the  $\tau$  values from Eqs. 10 and 11 can be used directly as the  $a$  and  $b$  terms in Eq. 12. The  $a$  term is the  $\tau$  condition based on the  $m$  and  $p$  conditions at the start of the element, and the  $b$  term is based on the  $m$  and  $p$  conditions at the end of the element.

$$[k] = \frac{EI}{L} \begin{bmatrix} \frac{12}{L^2} \left( \frac{a+b}{2} \right) & -\frac{6}{L} \left( \frac{2a+b}{3} \right) & -\frac{12}{L^2} \left( \frac{a+b}{2} \right) & -\frac{6}{L} \left( \frac{a+2b}{3} \right) \\ & 4 \left( \frac{3a+b}{4} \right) & \frac{6}{L} \left( \frac{2a+b}{3} \right) & 2 \left( \frac{a+b}{2} \right) \\ & & \frac{12}{L^2} \left( \frac{a+b}{2} \right) & \frac{6}{L} \left( \frac{a+2b}{3} \right) \\ \text{Sym.} & & & 4 \left( \frac{a+3b}{4} \right) \end{bmatrix} \quad (12)$$

The stiffness matrix in Eq. 12 is already a part of the nonlinear material capabilities of *MASTAN2* (2015). The computer program also contains incremental analysis routines for modeling the nonlinear geometric behavior. Eqs. 10 and 11 were implemented in a nonlinear material subroutine of *MASTAN2*. For a given wide-flange section, the constants  $\lambda$ ,  $\lambda_o$ ,  $\lambda_1$  and  $c_r$  were input, and for a given  $p$  condition, Eqs. 1 and 2 were used to evaluate  $m_1$  (the limit on the extent of  $\tau = 1$ ), Eqs. 3 and 5 were used to evaluate  $\tau_p$ , and Eqs. 6 through 9 were used to evaluate  $m_0$  (the boundary that defines  $\tau = 0$ ). With  $m_1$ ,  $\tau_p$  and  $m_0$  defined, the  $m$  condition at each end of the element was used to generate the  $a$  and  $b$  terms in Eq. 12.

##### 4.2 El-Zanaty portal frame

The El-Zanaty (1980) portal frame as depicted in Fig. 12 was modeled using *MASTAN2* with eight elements for all three members. Second-order inelastic analyses were conducted for conditions of  $c_r = 0.18$  and  $0.42$  to study the effect of residual stress on the ultimate load conditions of the frame under increasing magnitude of initial vertical load. The loading conditions were investigated by first applying the full vertical load  $P$ , then the lateral load  $H$  was applied in increments up to its maximum value when instability occurred in the columns. Both major axis bending and minor axis bending conditions were investigated using Eqs. 10 and 11 as the material model with the  $n$  values as given in Figs. 9 and 10. For this test frame condition, initial geometric imperfection was ignored.

Fig. 13 illustrates the effect of residual stress on the ultimate load response under increasing magnitude of initial vertical load. The  $x$ -axis is normalized by dividing the sum of the vertical loads by the sum of the column yield loads ( $p_i = \Sigma P / \Sigma P_y$ ). The  $y$ -axis is the relative percent

difference in the ultimate load  $H$  conditions and is calculated for a given  $p_i$  condition by dividing the difference between the ultimate load factor for  $c_r = 0.18$  and  $0.42$  by the average of the two load factors. Fig. 13 reveals a significant residual stress effect for the El-Zanaty frame for both the major axis bending and minor axis bending conditions. As  $p_i$  approaches the ultimate load condition due to the vertical loads only, the residual stress effect dramatically increases. For a given  $p_i$  condition, the magnitude of residual stress has a larger effect on the ultimate load condition for minor axis bending than for major axis bending.

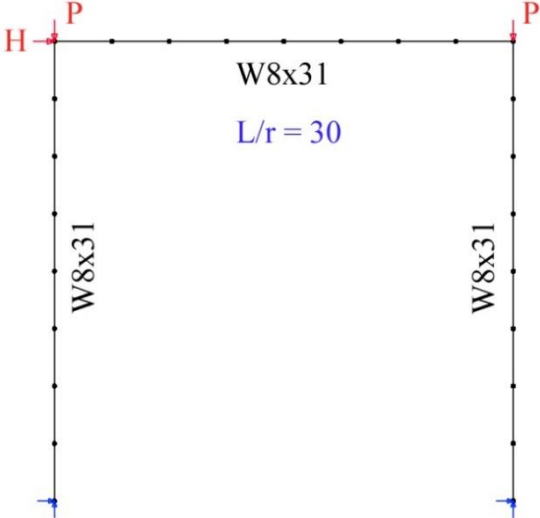


Figure 12: El-Zanaty portal frame model for both major and minor axis bending conditions

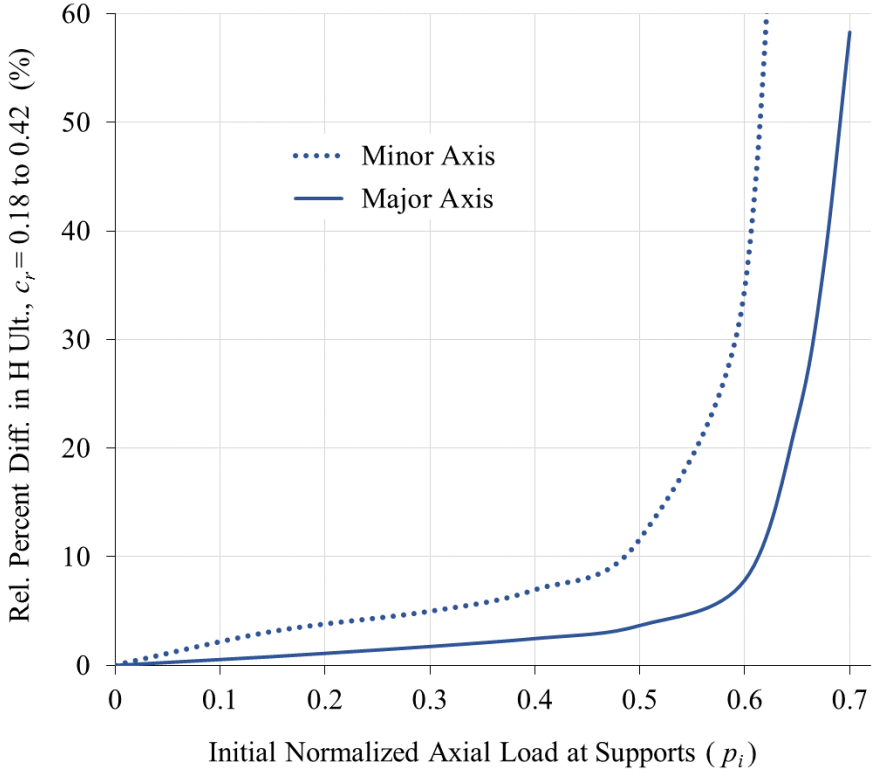


Figure 13: El-Zanaty frame relative percent difference in ultimate load H conditions for  $c_r = 0.18$  to  $0.42$

The El-Zanaty frame is particularly sensitive to second-order effects and nonlinear material behavior that leads ultimately to column instability. This frame explains the residual stress effect by considering the initial  $p$  in the columns and the different  $\tau_p$  stiffness condition for  $c_r = 0.18$  versus 0.42. When  $p > 1 - c_r$ , there is a precipitous drop in stiffness from  $\tau = 1$  to  $\tau_p$ , and as illustrated by comparing the purple lines in Fig. 3 with Fig. 4, this effect is more pronounced for minor axis bending than for major axis bending. When  $c_r = 0.42$  and  $p > 0.58$ , the column stiffness prior to H being applied is considerably less than the column stiffness when  $c_r = 0.18$  and the same  $p$  condition. When  $p < 0.58$ , there is no initial yielding of the columns prior to H being applied for both  $c_r$  conditions. Increments of lateral load eventually produce instability of the columns under a combination of axial compression and bending. At the lower values of  $p$ , stiffness reduction occurs primarily due to bending where the influence of  $c_r$  has less of an effect.

#### 4.3 Shayan test frames

Shayan *et al.* (2014) studied the effects of residual stress on the ultimate load capacity of four test frames by conducting nonlinear finite analyses. Three of their test frames were modeled using *MASTAN2* and the material model in Eqs. 10 and 11. Figs. 14 and 15 illustrate the number of elements and the member properties of Shayan's Frame 1 and Frame 2, respectively. Second-order inelastic analyses were conducted for conditions of  $c_r = 0.18, 0.24, 0.30, 0.36$  and 0.42 to study the effect of residual stress on the ultimate load conditions of each frame. Shayan investigated these two frames using only vertical loads ( $H = 0$ ) and major axis bending conditions. The  $m$ - $p$ - $\tau$  conditions of the 150UB14 were studied in detail using the same fiber element computer program as that used to study the W8x31. For both frames, initial geometric imperfection was modeled based on scaling the first eigenmode by the value of 0.00142L.

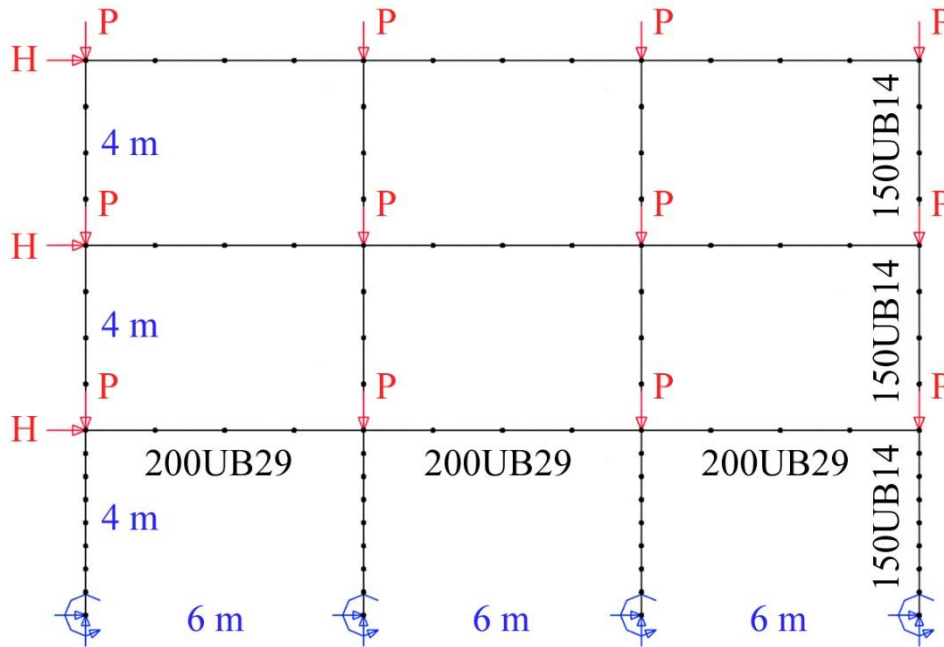


Figure 14: Frame 1 model ( $E = 200$  GPa,  $\sigma_y = 320$  MPa)

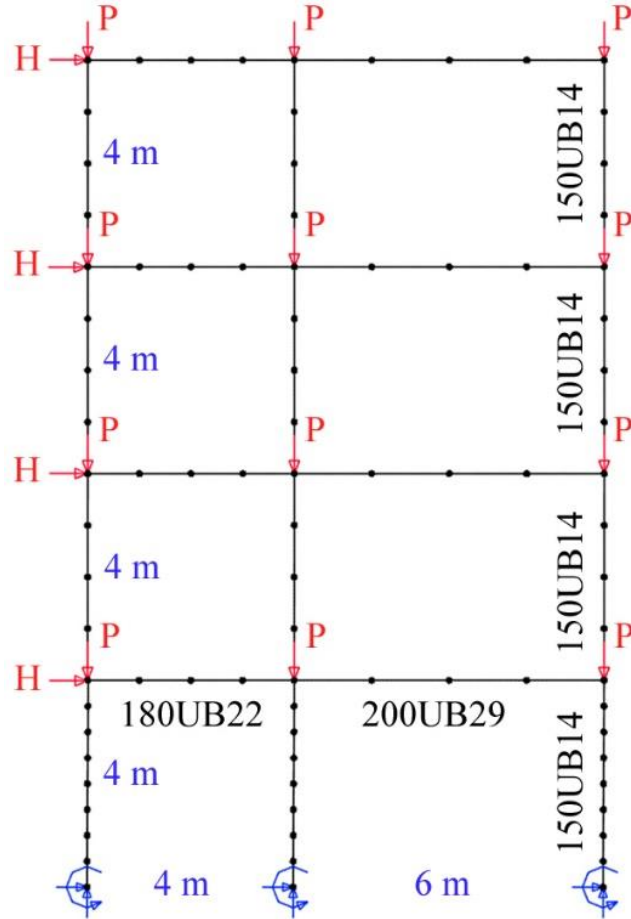


Figure 15: Frame 2 model ( $E = 200 \text{ GPa}$ ,  $\sigma_y = 300 \text{ MPa}$ )

Fig. 16 illustrates the stiffness reduction of the 150UB14 with residual stress conditions of  $c_r = 0.18, 0.30$  and  $0.42$  under major axis bending and axial compression. Comparing the stiffness reduction of the three  $c_r$  conditions, it is noticed that the greatest difference occurs under high axial load conditions when  $p > 1 - c_r$ . Eqs. 10 and 11 were used to approximate the fiber element data, and it was determined that  $n = 4$  provided the best fit. Nonlinear *MASTAN2* analysis results are given in Table 1 along with Shayan's finite element results. The results indicate that using  $n = 4$  gives slightly higher ultimate load factors; however, the relative percent difference results between  $c_r = 0.18$  and  $0.42$  are actually lower when using Eqs. 10 and 11 with  $n = 4$ . The relative percent difference for Frame 1 is 3.6% vs. Shayan's 9.3%, and for Frame 2 is 2.8% vs. Shayan's 9.4%.

Table 1: Ultimate load factor results for Frames 1 and 2

Major Axis	Frame 1		Frame 2	
	Shayan <i>et al.</i>	$n = 4$	Shayan <i>et al.</i>	$n = 4$
$c_r = 0$	1.454	1.450	1.154	1.178
$c_r = 0.18$	1.368	1.425	1.090	1.158
$c_r = 0.24$	1.339	1.415	1.065	1.152
$c_r = 0.30$	1.307	1.400	1.040	1.144
$c_r = 0.36$	1.277	1.390	1.016	1.136
$c_r = 0.42$	1.246	1.375	0.992	1.126

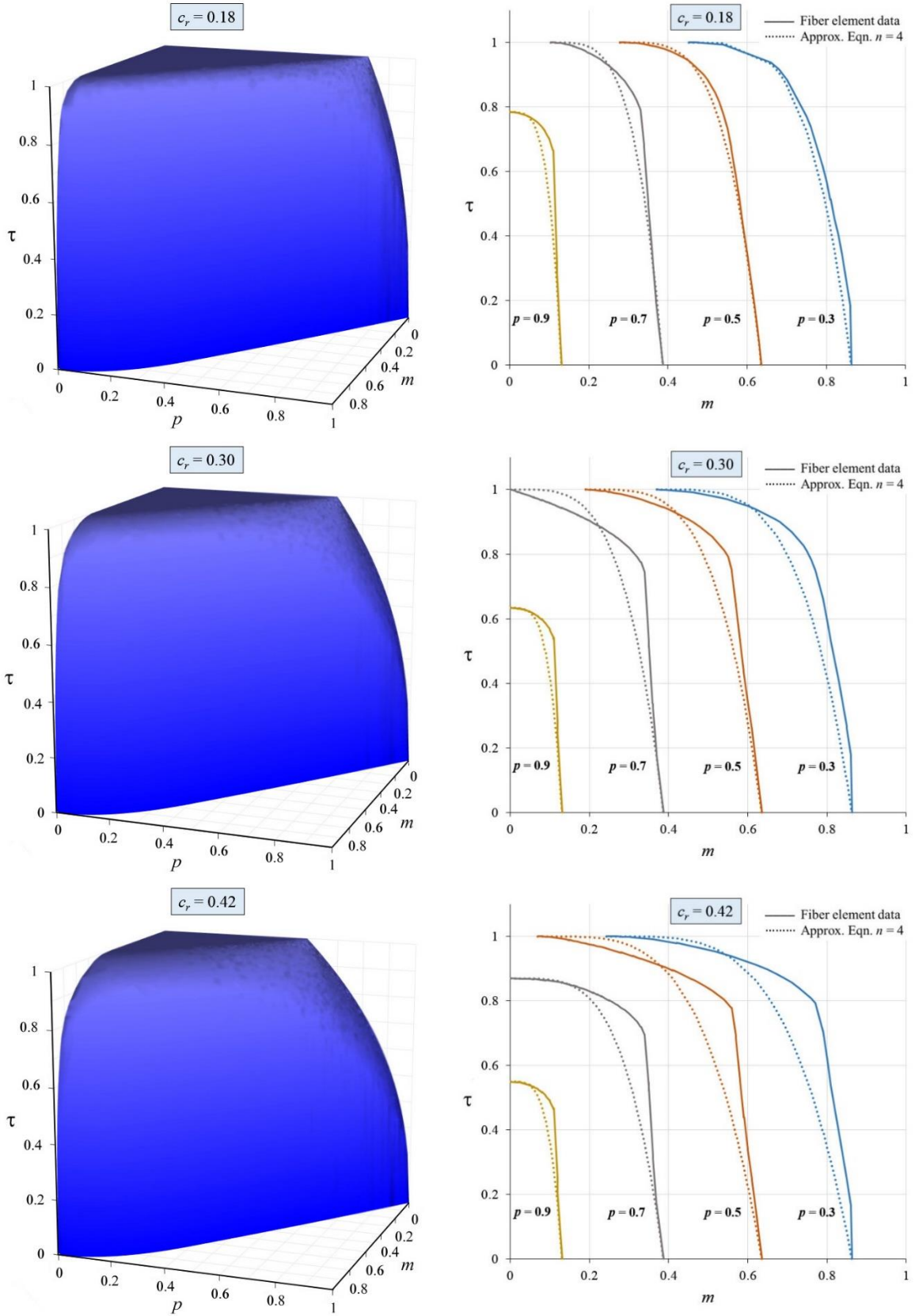


Figure 16: 150UB14 major axis bending and axial compression  $m$ - $p$ - $\tau$  conditions for  $c_r = 0.18, 0.30$  and  $0.42$

Both Frames 1 and 2 were studied further by first applying the vertical loads to a given magnitude, then the lateral loads were applied in increments up to their maximum value at which instability occurred. Using  $n = 4$  and the results for  $c_r = 0.18$  and  $0.42$ , Fig. 17 reveals a significant residual stress effect for both frames. As  $p_i$  approaches the ultimate load condition due to the vertical loads only, the residual stress effect dramatically increases. For  $p_i > 0.35$ , the magnitude of residual stress has a slightly larger effect on the ultimate load conditions for Frame 2 than for Frame 1.

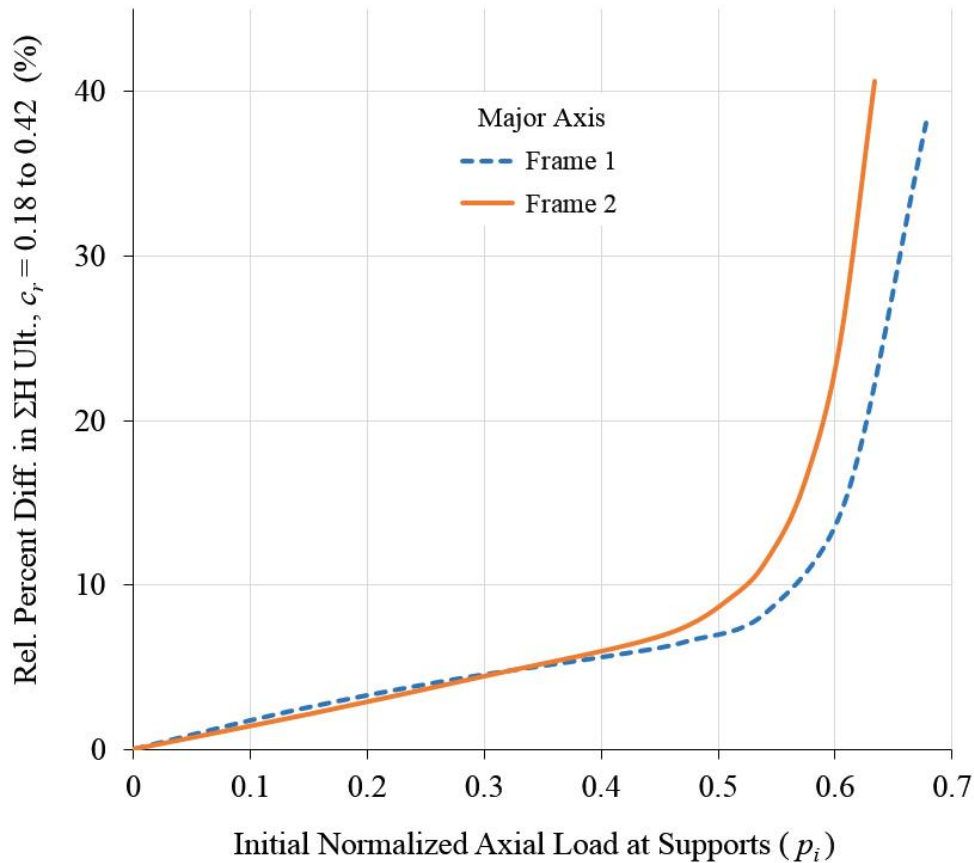


Figure 17: Frames 1 and 2 (Major Axis) relative percent difference in ultimate load  $\Sigma H$  conditions,  $c_r = 0.18$  to  $0.42$

Fig. 18 illustrates the  $m$ - $p$ - $\tau$  surface plots for the residual stress conditions of  $c_r = 0.18$  and  $0.42$  under minor axis bending and axial compression. Viewing the surface plot from this perspective, there is a significantly reduced triangular  $\tau = 1$  region when  $c_r = 0.42$  compared with  $c_r = 0.18$ , and there is a considerable loss of stiffness for a given increment increase in  $m$  when  $p > 1 - c_r$ . Comparatively, there is less difference between the two surfaces for the same increment increase in  $m$  when  $p \leq 1 - c_r$ .

Using  $n = 2$  and the results for  $c_r = 0.18$  and  $0.42$ , Fig. 19 also reveals a significant residual stress effect for both frames under minor axis bending conditions. As  $p_i$  approaches the ultimate load condition for each frame due to the vertical loads only, the residual stress effect dramatically increases. For  $p_i > 0.04$ , the magnitude of residual stress has a slightly larger influence on the ultimate load  $\Sigma H$  conditions for Frame 2 compared with Frame 1.

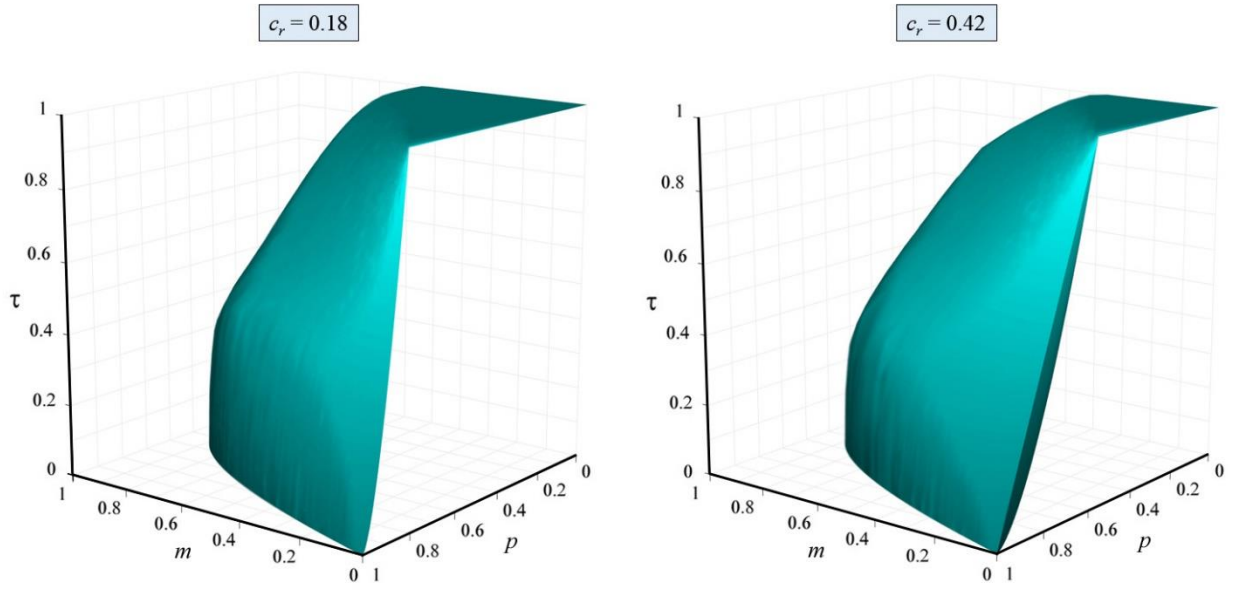


Figure 18: 150UB14 minor axis bending and axial compression  $m$ - $p$ - $\tau$  conditions for  $c_r = 0.18$  and  $0.42$

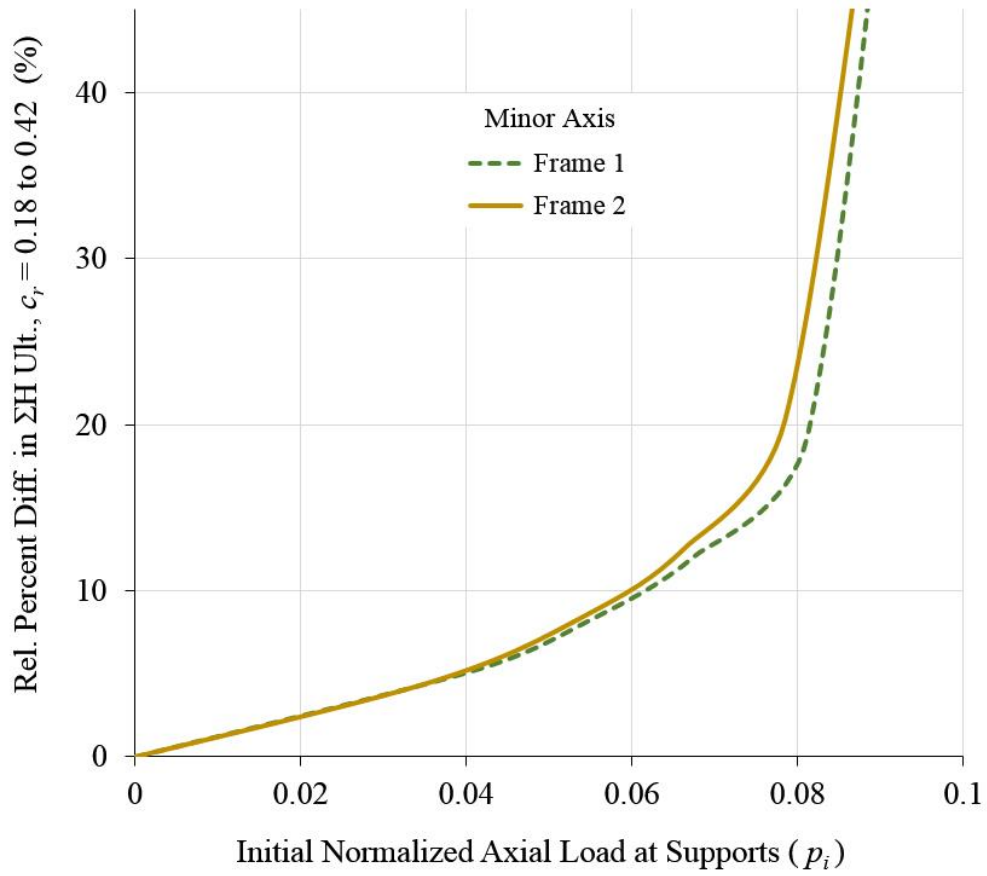


Figure 19: Frames 1 and 2 (Minor Axis) relative percent difference in ultimate load  $\Sigma H$  conditions,  $c_r = 0.18$  to  $0.42$

Shayan *et al.* (2014) investigated the structure in Fig. 20 to determine the effect of residual stress on a practical steel frame with a more realistic loading condition. Their study considered the vertical load to lateral load ratio of  $u/w = 12.5$  under major axis bending conditions and with both loads applied simultaneously. For the residual stress conditions of  $c_r = 0.18$  and  $0.42$ , they found a relative percent difference in the ultimate load factors to be 1.4%. The capacity of this frame for increased vertical loads allowed for an investigation of the residual stress effect up to 1.375 times the  $u$  value in their study. The current study considered higher  $u/w$  ratios by first applying a given magnitude of  $u$ , then  $w$  was applied using increments of load up to the collapse condition. Using Eqs. 10 and 11 in *MASTAN2*, the columns were modeled with  $n = 4$  and the beams with  $n = 2$ . Major axis bending was considered for all members, and initial geometric imperfection was modeled based on scaling the first eigenmode by the value of  $0.00142L$ .

Using the results for  $c_r = 0.18$  and  $0.42$ , Fig. 21 reveals a larger residual stress effect for higher  $u/w$  ratios as  $p_i$  approaches the ultimate load condition due to the vertical loads only. At the vertical load condition of  $1.375u$ , the relative percent difference in the lateral load at collapse is approximately 8%. Although this percentage is much higher than 1.4%, it is still considerably less than the relative percent difference results of the previous three test frames. The practical design example does however confirm that under high vertical load conditions the magnitude of the residual stresses has a more pronounced effect on the ultimate load capacity of the frame. Whereas the previous three test frames failed by instability of the bottom floor columns, the more practical frame failed due to a combination of both beams and columns reaching their ultimate strength capacities.

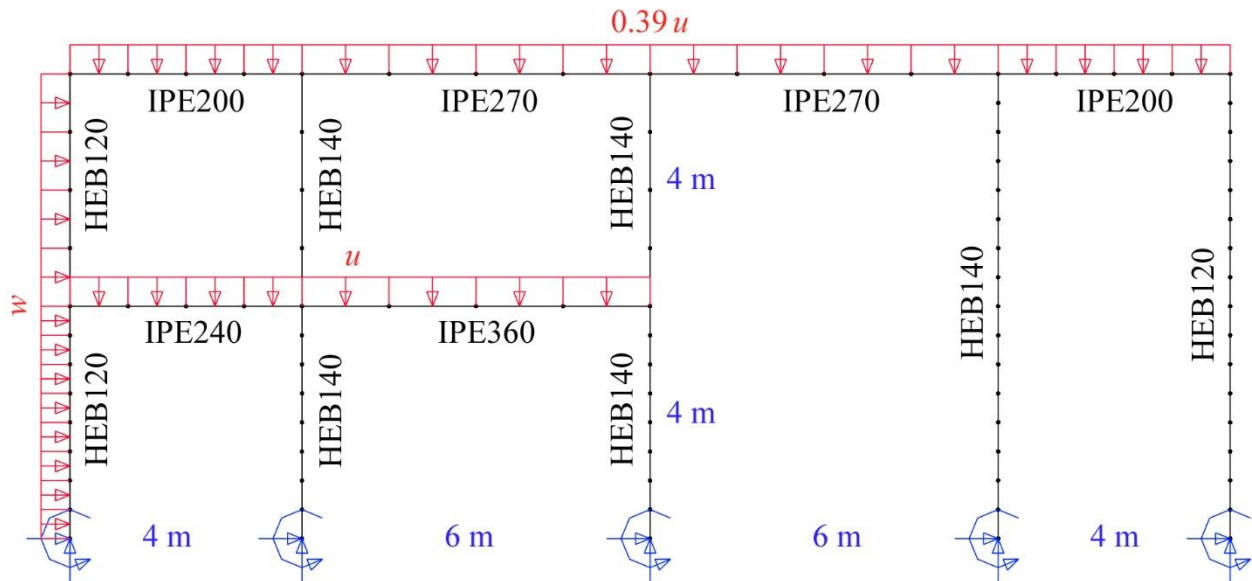


Figure 20: Frame 3 model ( $E = 210$  GPa,  $\sigma_y = 275$  MPa)

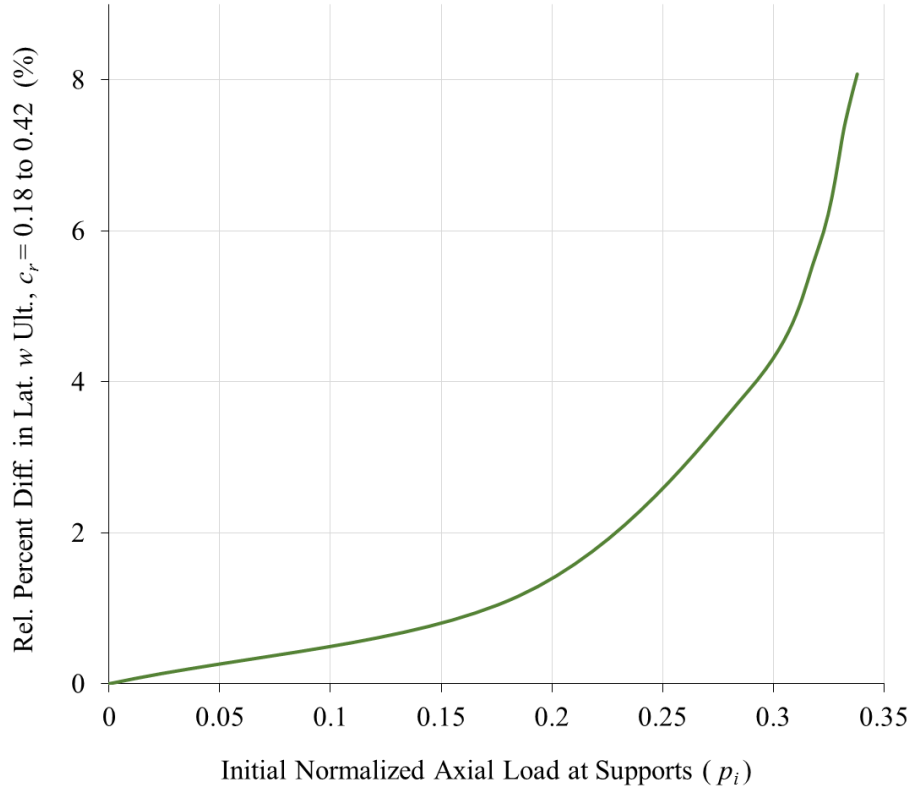


Figure 21: Frame 3 (Major Axis) relative percent difference in ultimate lateral load  $w$  conditions,  $c_r = 0.18$  to  $0.42$

## 5. Conclusions

This research focused on developing a deeper understanding of the effect the magnitude of residual stress has on the ultimate load conditions of steel frames. Based on the statistical study of scale factors for the ECCS residual stress pattern by Shayan *et al.* (2014), scale factors of 0.6 and 1.4 were used; thus the range of maximum residual stress varied between  $0.18\sigma_y$  and  $0.42\sigma_y$ . To approximate the stiffness reduction over the full range of  $m$ ,  $p$  and  $c_r$  conditions, a nonlinear material model was developed based on detailed fiber element model results. The stiffness reduction conditions between  $m_1$  and  $\tau_p$  to  $m_0$  are based on approximate nonlinear equations that can vary based on a given exponent  $n$  to account for the axis of bending and geometry of the cross-section. Since  $m_1$  and  $\tau_p$  are in the material model, the moment-curvature plots will always match the fiber element results in the linear region up to the initial yield conditions, and since  $m_0$  is also used, the approximate results will always converge to the fiber element results as the curvature increases under a given axial load condition. The approximate equations will always have more error associated with minor axis bending compared with major axis bending because there is a much larger variation in the minor axis bending  $m$ - $\tau$  curves for a given  $p$  condition.

Using the material model in *MASTAN2*, the El-Zanaty frame was used to explain the residual stress effect. It was found that as  $p_i$  approaches the ultimate load condition due to the vertical loads only, the residual stress effect dramatically increased. The magnitude of residual stress has a larger effect on the ultimate load conditions for minor axis bending than for major axis bending. This is because there is a significant loss in stiffness from  $\tau = 1$  to  $\tau_p$  when  $p > 1 - c_r$ , and this effect is more

pronounced for minor axis bending than for major axis bending. When  $p \leq 1 - c_r$ , there is no initial yielding of the columns prior to H being applied, and eventually with increments of lateral load loss of stiffness occurs under a combination of axial compression and bending. At these lower values of  $p$ , stiffness reduction occurs primarily due to bending where the influence of  $c_r$  has less of an effect. Two additional test frames with concentrated loads at the beam-to-column joints produced similarly significant residual stress effects as  $p_i$  approaches the ultimate load condition due to the vertical loads only. A final test frame was used to determine the effect of residual stress on a practical steel frame with a more realistic loading condition. The residual stress effect was found to be less significant for this frame as the loss of stiffness occurred in both the beams and columns primarily due to bending. All four test frame results confirmed that under increasing vertical load conditions, the magnitude of the residual stresses has more of an effect on the ultimate load capacity of the frame.

## References

- Attalla M.R., Deierlein G.G., McGuire W. (1994). "Spread of plasticity: quasi-plastic-hinge approach." *Journal of Structural Engineering*, 120 (8) 2451-2473.
- Ban H., Shi G., Shi Y., Wang Y. (2012). "Overall buckling behavior of 460 MPa high strength steel columns: Experimental investigation and design method." *Journal of Constructional Steel Research*, 74: 140–150.
- Ban H., Shi G., Shi Y., Bradford M. (2013). "Experimental investigation of the overall buckling behaviour of 960 MPa high strength steel columns." *Journal of Constructional Steel Research*, 88: 256–266.
- Beedle L.S., Tall L. (1962) "Basic column strength." *Transactions of the ASCE*, 127:138–179.
- Chen W.F., Sohal I. (1995). *Plastic design and second-order analysis of steel frames*. Springer-Verlag, New York.
- ECCS (1984). "Ultimate limit state calculation of sway frames with rigid joints." *TC 8 of European Convention for Constructional Steelwork (ECCS)*, No. 33.
- El-Zanaty M.H., Murray D.W., Bjorhovde R. (1980). "Inelastic behavior of multistory steel frames." *Structural Engineering Report No. 83*, University of Alberta, Edmonton, Alberta, Canada.
- Gardner L., Bu Y., Theofanous M. (2016). "Laser-welded stainless steel I-sections: Residual stress measurements and column buckling tests." *Engineering Structures* 127: 536–548.
- Huber A.W., Beedle L.S. (1954). "Residual stress and the compressive strength of steel." *Welding Journal*, 33 (12) 589-s, Fritz Laboratory Reports, Paper 1510.
- Kucukler M., Gardner L., Macaroni L. (2014). "A stiffness reduction method for the in-plane design of structural steel elements." *Engineering Structures*, 73: 72-84.
- Kucukler M., Gardner L., Macaroni L. (2016). "Development and assessment of a practical stiffness reduction method for the in-plane design of steel frames." *Journal of Constructional Steel Research*, 126: 187-200.
- Rosson B.T. (2016). "Elasto-plastic stress states and reduced flexural stiffness of steel beam-columns." *Proceedings of the 2016 SSRC Annual Stability Conference*, Orlando, Florida.
- Rosson B.T. (2017). "Major and minor axis stiffness reduction of steel beam-columns under axial compression and tension conditions." *Proceedings of the 2017 SSRC Annual Stability Conference*, San Antonio, Texas.
- Shayan S., Rasmussen, K.J.R., Zhang, H. (2014). "Probabilistic modeling of residual stress in advanced analysis of steel structures." *Journal of Constructional Steel Research*, 101: 407-414.
- Shi G., Ban H., Bijlaard F.S.K. (2012). "Tests and numerical study of ultra-high strength steel columns with end restraints." *Journal of Constructional Steel Research*, 70: 236–247.
- Spoorenberg R.C., Snijder H.H., Hoenderkamp J.C.D. (2011). "Proposed residual stress model for roller bent steel wide flange sections." *Journal of Constructional Steel Research*, 67: 992–1000.
- Ziemian R.D., McGuire W. (2002). "Modified tangent modulus approach, a contribution to plastic hinge analysis." *Journal of Structural Engineering*, 128 (10) 1301-1307.
- Ziemian R.D., McGuire W. (2015). *MASTAN2*, Version 3.5.
- Zubydan A.H. (2011). "Inelastic second order analysis of steel frame elements flexed about minor axis." *Engineering Structures*, 33: 1240-1250.